Optik - International Journal for Light and Electron Optics 169 (2018) 277–290

Contents lists available at ScienceDirect

Optik

journal homepage: www.elsevier.com/locate/ijleo

Research on deployable heat dissipation lens hood technology of geostationary optical remote sensor

Guan Fengwei[a,b,*], Zhang Feng[a], Cao Nailiang[a,b], Zhao Qinglei[a], Wang Shuxin[a], Guan Hongyu[a], Yu Shanmeng[a], Liu Ju[a]

[a] Changchun Institute of Optics, Fine Mechanics and Physics, Chinese Academy of Sciences, Changchun, 130033, China
[b] University of Chinese Academy of Sciences, Beijing, 100049, China

ARTICLE INFO

Keywords:
Geostationary
Optical remote sensor
Deployable
Heat dissipation
Lens hood

ABSTRACT

In order to deter direct sunlight from coming into contact with the light aperture of geostationary optical remote sensor, an in-orbit deployable heat dissipation lens hood was designed, and the optical-thermal characteristics and structural characteristics of the proposed lens hood were analyzed and tested. First, the special thermal environment of geostationary optical remote sensor was analyzed to determine the design requirements of the lens hood. After that, a deployable heat dissipation lens hood with inner diaphragms was designed and a prototype was made. Then, the optical-thermal characteristics of the lens hood were analyzed by ray tracing and heat flux calculation, and the structural characteristics of the lens hood were analyzed through mechanical simulation. Finally, a functional test was carried out on the prototype, and the dynamic stiffness was tested in the compression locked state. The results show that the lens hood can significantly improve the optical-thermal characteristics of the optical system and meet the overall dynamic stiffness requirements.

1. Introduction

A geostationary optical remote sensor features wide field of view, long monitoring time, and time-lapse fixed-point shooting can theoretically cover most of the earth's surface with a network of three satellites. Coupled with low light level and infrared imaging technology, the sensor will be capable of all-weather reconnaissance. High-orbit optical remote sensors have been developed worldwide for use in meteorological forecasting applications, environmental protection, land survey, etc. For instance, China launched Gaofeng-4 (GF-4) geostationary satellite into space in 2015. With ground resolution for visible light imager at 50 m and for the infra-red payload at 400 m, this satellite is the most advanced geostationary remote sensing satellite. Of course, there is still much room for improvement regarding its main performance indicators. Remote satellites of a larger diameter and higher resolution are currently in development. On geosynchronous orbit, a space optical remote sensor experiences complex, alternating external heat flux. The optical port of the camera faces direct sunlight in nearly half of the orbital period, especially at around midnight. The incident energy entering the optical system will lead to significant temperature fluctuation inside the optical and mechanical structure. The stray light of the optical system will increase dramatically, which seriously degrades the image quality. Therefore, light aperture sun shielding is an indispensable technology for geostationary optical remote sensors. Nevertheless, it is very difficult to design the sun shielding component for a large-diameter optical system. Taking the 1.5 m diameter optical system as an example, the

* Corresponding author at: Changchun Institute of Optics, Fine Mechanics and Physics, Chinese Academy of Sciences, Changchun, 130033, China; University of Chinese Academy of Sciences, Beijing, 100049, China.
E-mail address: buaaguan@sina.com (F. Guan).

https://doi.org/10.1016/j.ijleo.2018.05.027
Received 20 March 2018; Accepted 8 May 2018

required sun shielding component has to be almost 10 m in length to completely prevent the sun exposure, which is far beyond the carrying capability of the size of a typical rocket fairing. As a result, it is imperative to develop a lens hood for the light aperture which can be deployed in orbit.

The application of deployable mechanism is traced back to the 1970s. The past four decades have witnessed the mechanism being extensively utilized in space science, ranging from the unfolding of solar panels, the deployment of communication antennas, space arm, to various lunar and Mars probes. Based on the deployment dimension, the deployable mechanism is divided into single point hinge deployable mechanism [1,2], one-dimensional deployable mechanism [3,4], two-dimensional deployable mechanism [5–7], and three-dimensional deployable mechanism. Some space observing systems have adopted the deployable sunshield, such as the PROGNOZ series of early warning satellites [8], the James Weber Space Telescope (JWST) [9], the SBIRS GEO satellites [10], the GAIA satellite [11,12], the MITAR satellite [13,14], the International X-ray Observatory (IXO) [15], and Astrium's GO-3S satellite [16], to name but a few.

For the geostationary orbit optical remote sensor, two major technical problems must be resolved in the development of an in-orbit deployable light aperture lens hood: the driver of the deployable mechanism, and the configuration after deployment. The deployment mechanism is driven by a motor, spring [17,18], self- extension [19], inflation [20–22], elastic recovery [23,24],sleeve screw. The deployment mechanism compresses and locks down the lens hood before the launch, and expands the lens hood to the preset shape after entering into orbit. After deployment, the configuration of the lens hood prevents direct sunlight from coming into contact with the optical system, and reduces the incident energy entering the lens hood. To avoid direct exposure to sunlight, the lens hood configuration must be designed with consideration for the space environment and external heat flux in the geosynchronous orbit, and in view of such parameters of the optical remote sensor such as diameter, field angle, etc. In addition to the avoidance of direct exposure to the sun, the incident energy must also be reduced because the energy entering the lens hood system will cause strong heat retention, resulting in significant temperature fluctuation within the optical and mechanical structure. The commonly used incident energy reduction technologies include rotatable servo lens hood, stagewise lens hood, cellular inner wall lens hood, etc. The rotatable servo lens hood must rotate with the incident angle of sunlight during orbit, and therefore has very high reliability requirements. The stagewise lens hood is mainly used on fixed structures. The cellular inner wall lens hood is arranged vertical vanes to suppress stray light. However, there has been no definite report on the deployable heat dissipation lens hood proposed in this paper for the optical port of geostationary optical remote sensor.

2. Analysis of the deployable lens hood

2.1. Analysis of working conditions

When the space optical remote sensor is in orbit, the camera is often under the combined action of solar irradiation, earthshine, and terrestrial infrared radiation. However, if the remote sensor moves in a geosynchronous orbit, the camera's temperature is mainly affected by the external heat flux of direct solar radiation. In this case, the earthshine and terrestrial infrared radiation are small enough to be ignored. Hence, the camera is significantly impacted by continuously changing solar heat flux.

According to the relative position of the sun, the earth and the satellite, the typical working points of the satellite in orbit are the spring and autumn equinox, and the summer and winter solstice, when the sun shines directly over 8.7° north latitude, and when the sun shines directly over 8.7° south latitude. With the typical working conditions, this author divides the position of the sun in a year and displays the relative locations in space of the sun, the earth and the satellite, as shown in Fig. 1.

Based on the position of the sun, this author analyzes how the solar angle of incidence changes throughout the year:

a) The spring and autumn equinox.
When it is night at local mean time, the relationship between the opening of the camera's aperture and the position of the sun is shown in Fig. 2.
Let φ be the camera's field angle, θ the angle between the camera axis and the sun direction, L the length of the camera interior

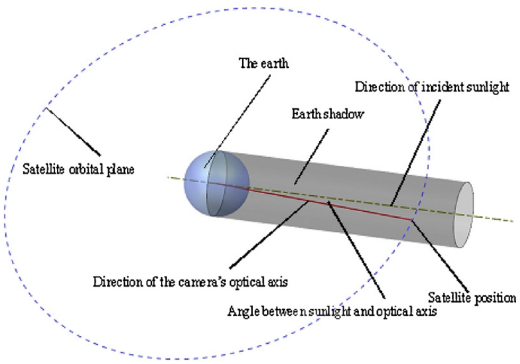

Fig. 1. Relative locations in space.

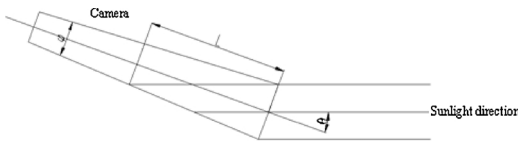

Fig. 2. Relationship between the camera's aperture and the position of the sun.

touched by the sunlight, and D the diameter of the light aperture on the lens hood. Then there is the following relationship:

$$L = \frac{D}{\tan\theta + \tan\frac{\phi}{2}} \tag{1}$$

When the satellite moves to the boundary point of the "earth shadow", θ reaches the minimum. At this time, the camera light aperture plane experiences the strongest solar radiation, and the length camera interior touched by the sunlight L is the longest. Fig. 3 illustrates the relative locations of the sun's direction, the earth and the camera.

When the satellite moves to the boundary point of the earth's shadow, the following is obtained according to the spatial geometrical relations between the sun, the earth and the camera:

$$\theta = \arcsin\frac{R}{R+H} = \arcsin\frac{6371}{42157} \approx 8.7° \tag{2}$$

Where R is the earth radius, and H is the orbital height.

b) The summer and winter solstice.
When it is midnight at local mean time during the summer and winter solstices, the angle between the sun's direction and the camera's optical axis reaches the minimum at 23.5°. At this time, the camera is under the strongest surface solar radiation.

c) 8.7° north/south latitude.
When the sun shines directly over 8.7° north/south latitude, the working orbit of the camera reaches the boundary point of the "earth shadow". With the sun in this position, when it is midnight at local mean time, the angle between the sun's direction and the camera's optical axis reaches the minimum at 8.7°. At this time, the camera is exposed to the strongest surface solar radiation.

d) Between 8.7° north latitude and the summer solstice.
When the sun shines directly over the region between 8.7° north latitude and the summer solstice, the satellite always stays outside the "earth shadow". Based on the analysis in the above sections, it is found that the angle between the sun's direction and the camera's optical axis increases monotonically from 8.7° to 23.5° when the sun shines directly over the region between 8.7° north latitude and the summer solstice.

e) Between 8.7°south latitude and the winter solstice.
When the sun shines directly over the region between 8.7° south latitude and the winter solstice, the satellite always stays outside the "earth shadow". Based on the analysis in the above sections, it is found that the angle between the sun's direction and the camera's optical axis increases monotonically from 8.7° to 23.5° when the sun shines directly over the region between 8.7° south latitude and the winter solstice.

f) Between the spring equinox and 8.7° north latitude.
It can be seen from the relative locations in Fig. 1 that the minimum angle between the sun direction and the camera's optical axis is 8.7° when the sun shines directly over the region between the spring equinox and 8.7° north latitude.

g) Between the autumn equinox and 8.7° south latitude.
When the sun shines directly over the region between the autumn equinox and 8.7° south latitude, the relative locations of the

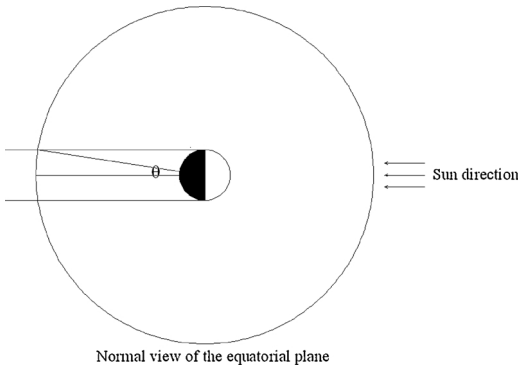

Fig. 3. Relative locations of the sun, the earth and the camera at the earth's shadow.

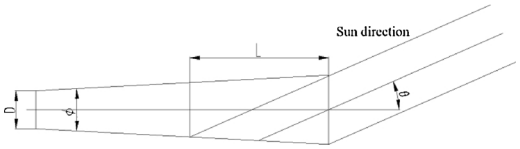

Fig. 4. Relationship between the inner surface contour of the lens hood and the sun direction.

sun, the earth, the orbital surface and the satellite are the same with those when the sun shines directly over the region between the spring equinox and 8.7° north latitude. The minimum angle between the sun's direction and the camera's optical axis is 8.7° when the sun shines directly over the region between the autumn equinox and 8.7° south latitude.

2.2. Lens hood requirements

The above sections provide an analysis of the working conditions of the geostationary space camera. According to the analysis, it can be seen that the first requirement of the lens hood is to prevent direct sunlight on the optical system. Heat will accumulate rapidly in the parts directly exposed to the sun, resulting in a sharp rise in temperature and creating much stray light.

According to the analysis of the working conditions, the angle between the sun's direction and the camera's optical axis is minimized at 8.7° when it is around midnight in a day and when the sun shines directly over the region between 8.7° north latitude and 8.7°south latitude in a year. The required length of the deployable lens hood can be determined in light of the angle, the field angle, and the diameter of the optical system.

As shown in Fig. 4, D is the diameter of the camera, φ is the camera's field angle, L is the length of the lens hood, and θ is the angle between the camera's optical axis and the sun's direction. Thus, there is the following relationship:

$$L = \frac{D}{\tan\left(\theta + \frac{\phi}{2}\right) - \tan\frac{\phi}{2}} \tag{3}$$

In the actual design, the lens hood length must be selected in consideration of the following principles:

- Ensure that the optical components are not exposed to direct sunlight;
- Meet the requirements of temperature and temperature difference for the camera's optical and mechanical structure;
- Shorten the lens hood through a sunlight avoidance maneuver of the satellite under the premise of ensuring the temperature stability of the camera;
- After compression, the lens hood should fit the fairing size.

2.3. Sunlight avoidance strategy of the satellite

At around midnight, the geostationary satellite usually makes a sunlight avoidance maneuver. The strategy lowers the design requirements on the lens hood assembly and makes it possible to design a shorter lens hood. The sunlight avoidance strategy is directly correlated with the β angle (the angle between the sun's direction and the equatorial plane), the camera diameter D, the camera's field angle φ, and the length of the lens hood L. Fig. 5 shows the variation of the β angle of the geostationary satellite in a year.

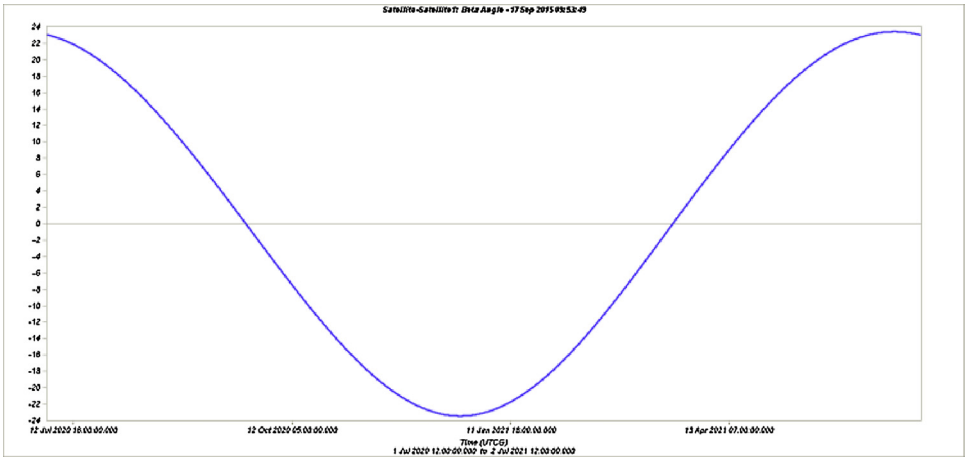

Fig. 5. Variation of the β angle of the geostationary satellite in a year.

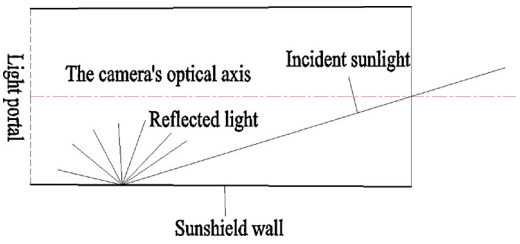

Fig. 6. Configuration of an ordinary lens hood after deployment.

Taking the 1.5 diameter optical system as an example, if $0 \le |\beta| < \arctan\frac{1.5}{L} + \frac{\phi}{2}$, the sunlight will enter the camera directly and the satellite should move sideways. When the sun shines directly over the northern hemisphere, the satellite should move sideways by $(\arctan\frac{1.5}{L} + \frac{\phi}{2}) - |\beta|$ degrees into the +Y direction between $\frac{\arctan\frac{1.5}{L}+\frac{\phi}{2}}{360} \times 24 \times 60$ min before midnight at local meantime to $\frac{\arctan\frac{1.5}{L}+\frac{\phi}{2}}{360} \times 24 \times 60$ min after midnight. When the sun shines directly over the southern hemisphere, the satellite should move sideways by $(\arctan\frac{1.5}{L} + \frac{\phi}{2}) - |\beta|$ degrees to the –Y direction between $\frac{\arctan\frac{1.5}{L}+\frac{\phi}{2}}{360} \times 24 \times 60$ min before midnight at local mean time to $\frac{\arctan\frac{1.5}{L}+\frac{\phi}{2}}{360} \times 24 \times 60$ min after midnight. When $\arctan\frac{1.5}{L} + \frac{\phi}{2} \le |\beta| \le 23.5°$, it is not necessary for the satellite to maneuver.

3. Design plan

3.1. Design philosophy

The lens hood is designed to suppress stray light and improve thermal characteristics of geostationary optical remote sensor. The diameter, the opening angle, the length and other parameters of the lens hood are directly related to the parameters of the optical system and the spatial environment. Based on the analysis of the working conditions in the preceding section, this author determines the inner diameter and opening angle of the lens hood according to the parameters of the optical system, and then sets the length of the lens hood in light of the in-orbit conditions.

The ordinary lens hood is designed in consideration of the parameters of the optical system. Fig. 6 illustrates the configuration of the ordinary lens hood after deployment.

Despite the prevention of direct sunlight on the optical system, the ordinary lens hood fails to effectively control the stray light produced by the light reflected to the interior of the optical system by the inner surface of the lens hood. Additionally, the temperature will rise drastically in the parts of the lens hood's inner surface experiencing direct sunlight. The sharp temperature rise poses a strong disturbance to the temperature level and temperature uniformity of the optical system.

Therefore, a diaphragm (a hollow opaque optical element that acts as a restraint on the incident light) lens hood is developed based on similar design parameters. In accordance with design inputs, this author carries out detailed design and analysis of inclination angle, height, spacing, stages, and surface properties of the diaphragm. Fig. 7 shows the diaphragm lens hood after deployment.

For the diaphragm lens hood depicted in Fig. 7, the inner contour shown in dashed lines is the same as that of a common lens hood, and the outer contour is dependent on the design constraints of the optical system. The lens hood has multi-stage diaphragms. At each stage, the surface of the diaphragm is a circular truncated cone. The inclination angle, height and spacing of the diaphragm differ from stage to stage. Featuring a high reflectance (≥ 0.95) on the illuminated side and high absorptivity (≥ 0.9) and high emissivity (≥ 0.9) on the back, the diaphragm can directly reflect the incident sunlight. It can either directly reflect a portion of the incident light out of the lens hood system, or move a portion of the incident light forward. In this way, it significantly weakens the thermal disturbance caused by incident sunlight to the optical system, and suppresses the stray light.

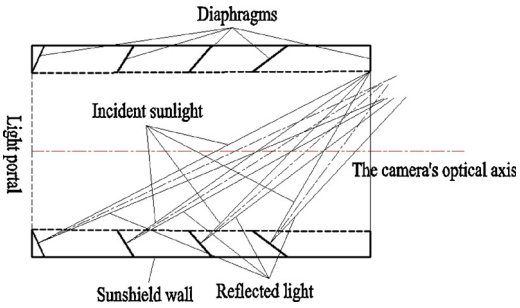

Fig. 7. Configuration of the diaphragm lens hood after deployment.

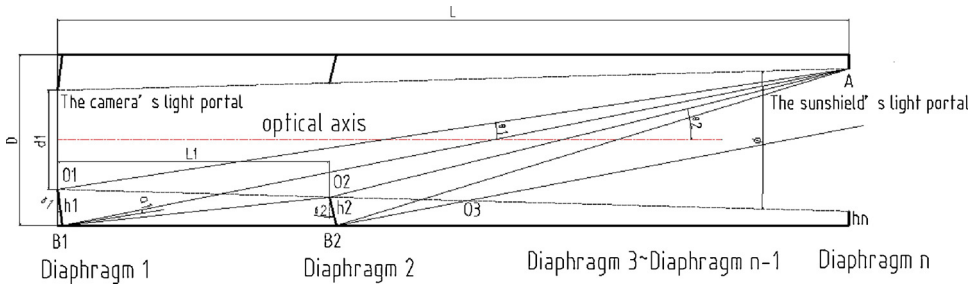

Fig. 8. Relative location of the multi-stage diaphragm in the lens hood.

When the camera is moving in orbit, the angle of incidence is constantly changing throughout a daily cycle, and with the four seasons of the year. Each stage of the diaphragms has a different effect on the incident light coming from various angles. A single-stage diaphragm mainly reflects the incident light coming from a certain angle range. As the diaphragm directly reflects a portion of the incident light within the range out of the lens hood system and reflects the rest of the light to the front of the lens hood, excellent effect of light extinction and heat dissipation are achieved in the optical system.

3.2. Overall design

The lens hood is extended along the optical axis of the optical system. Without considering the field angle, the inner contour diameter of the lens hood remains unchanged during the deployment process and is the same as the diameter of the optical system. However the diameter of the outer contour of the lens hood is limited by the size of the optical system and the space of the rocket fairing. After deployment, the outer contour and the inner contour of the lens hood should have the same length.

The diaphragm is a key component for improving the thermal characteristics of the optical system and for suppressing the stray light in the system. It should be capable of suppressing the deepest incident light: i.e. the light with a minimum of θ. Fig. 8 shows the relative location of the multi-stage diaphragms in the lens hood.

The diaphragm is designed stage-by-stage from Diaphragm 1 at the light aperture of the camera all the way to Diaphragm n at the light aperture of the lens hood. The light aperture of the camera in the lens hood has an inner diameter of d_1, an outer diameter of D, a total length of L, and a field angle of Φ. The surface of the diaphragm is a circular truncated cone. The side of diaphragm facing the light aperture of the lens hood has high reflectance (≥ 0.95) and low absorptivity (≤ 0.05). The inclination angle, height, spacing and stages of the diaphragm should be further designed step by step.

For Diaphragm 1, the incident light comes from the range from AO_1 to AB_1, the maximum angle of incidenceAO_1B_1 is 90°, the angle with respect to the optical axis is θ_1, the reflected light falls within the range between O_1A and B_1O_2. For Diaphragm 2, the incident light comes from the range from AO_2 to AB_2, the reflected light falls within the range between O_2A and B_2O_3, the maximum angle of incidenceAO_2B_2 is also 90°, the angle with respect to the optical axis is θ_2. The parameters of Diaphragm 3 to Diaphragm n-1 are deduced by analogy. For Diaphragm n at the light aperture of the lens hood, it is perpendicular to the optical axis of the camera and $[D-(d_1+2L\tan\Phi/2)]/2$ in height (h_n).

According to the geometric relationship in the figure, the inclination angle, height and other parameters of the diaphragm can be obtained stage-by-stage.

For Diaphragm k($2 \leq k \leq n-1$), the inclination angle θ_k is:

$$\delta_k = \theta_k = \arctan\left(\frac{L\tan\frac{\phi}{2} + d_{k-1} + L_{k-1}\tan\frac{\phi}{2}}{L - L_{k-1}}\right) \tag{4}$$

Where: $L_{k-1} = \frac{h_{k-1}\sin\delta_{k-1}\tan(\delta_{k-1}-\alpha_{k-1}) + \frac{D-d_{k-1}}{2}}{\tan(\delta_{k-1}-\alpha_{k-1}) + \tan\frac{\phi}{2}}$;

$$\alpha_{k-1} = 90° - \arctan\left(\frac{d_{k-1} + L\tan\frac{\phi}{2}}{h_{k-1}\sin\theta_{k-1}}\right)$$

Hence, the height of Diaphragm k is:

$$h_k = \frac{\frac{D-d_{k-1}}{2} - L_{k-1}\tan\frac{\phi}{2}}{\cos\delta_k} \tag{5}$$

With a purpose of avoiding sunlight, the diaphragm should be designed according to the above procedures. The parameters of the inclination angle, height, and spacing of the diaphragm are determined in light of the constraint conditions of the inner and outer contours of the lens hood. If the camera's light aperture diameter is 1.5 m, without taking into account the field angle or other parameters of the optical system, when the satellite moves ± 25° to avoid sunlight at around midnight, the lens hood configuration and diaphragm parameters are adjusted accordingly. Table 1 lists the parameters of the diaphragm in the sunlight avoidance posture according to the above procedures.

Table 1
Parameters of the diaphragm in the sunlight avoidance posture.

Name	Stage	Inclination angle δ/°	Height h/m	Spacing L/cm
Diaphragm1	Stage 1	25.00	28.69	81.64
Diaphragm 2	Stage 2	32.01	30.13	66.98
Diaphragm 3	Stage 3	41.11	33.41	60.48
Diaphragm 4	Stage 4	53.40	41.64	112.13
Diaphragm 5	Stage 5	0	24.65	–

The lens hood is supported by diaphragms and the deployment rod. Made of flexible materials, the lens hood wall is in the compressed state before the satellite enters the orbit. Driven by the deployment structure, the wall is gradually extended after the satellite settles into orbit. The compressed walls of the lens hood are shown in Fig. 9.

The inner surface of the wall is coated with a thick black cloth of low reflectivity (Reflectance ≤ 0.05), while the outer surface of the wall is coated with a white polyimide cloth of low absorptivity (emissivity ≥ 0.8, absorptivity ≤ 0.2). The surface properties will not change when the inner surface and outer surface films are folded. The interlayer is a multi-layer insulation component consisting of ten units. Each unit contains a layer of 6 μm-thick double-sided aluminum polyester film and a layer of polyester mesh. The perforation rate of the multi-layer insulation component is approximately 0.55% of the total area. The Φ1.8 mm diameter pores are separated from each other by 1.5 cm horizontally and 3 cm vertically.

3.3. Deployment mechanism

Fig. 10 shows the design of the deployment mechanism. The stage 1 sleeve is fixed, and the wire of the stage 2 sleeve is fixed to the stage 1 sleeve on the one end through a pulley, and to the roll of the motor on the other end. When the motor rotates, the roll begins to wind up the wire and thus pulls out the stage 2 sleeve. Because the wire of the stage 3 sleeve is also fixed to the stage 1 sleeve by the pulley assembly, the stage 3 sleeve will also be pulled out when the stage 2 sleeve is being pulled out. The design process is highly flexible because the number of layers of sleeves can be determined according to actual needs.

Fig. 11 shows the lens hood in its folded and extended status. The wire of the stage 1 sleeve is fixed to the roll of the motor. Driven by the motor, the sleeves of all stages will be unfolded simultaneously.

4. Optical-thermal characteristics analysis

4.1. Ray tracing

The trajectory of the incident energy entering the lens hood system is analyzed by Tracepro [25] to evaluate the optical-thermal characteristics of the lens hood. Firstly, this author constructs a model according to the configuration of the lens hood after deployment. The model only deals with the interior of the lens hood and does not take the components outside the light path into consideration. Apart from the model, the simulation requires a light source and a detector. The sunlight is simulated with a surface light source, and the reflected light intensity at the light aperture of the lens hood and the light intensity at the light aperture of the camera are measured with two hemispherical detectors. Fig. 12 shows the overall calculation and simulation process.

The number of incident photons entering the lens hood is 250,919, carrying a total energy of 250,919 W. The initial energy of each ray of the light source is set as 1 W. The reflectivity of the illuminated surface of the diaphragm is 0.95, the absorptivity of the other surfaces inside the lens hood is 0.9, and the incidence angle of the sun is 25°.The trajectories of all rays are displayed in Fig. 13.

The polar coordinates of the energy received by the detector are shown in Fig. 14, where the radial coordinates represent the

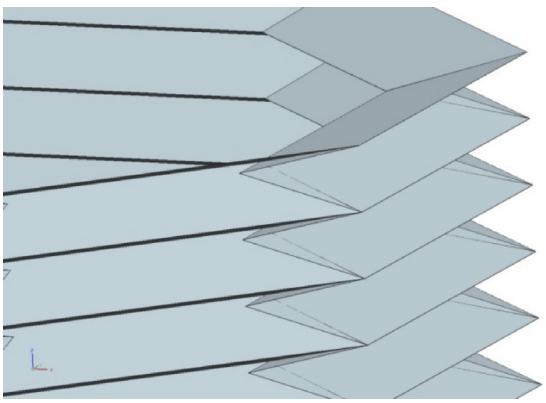

Fig. 9. Lens hood wall in the compressed state.

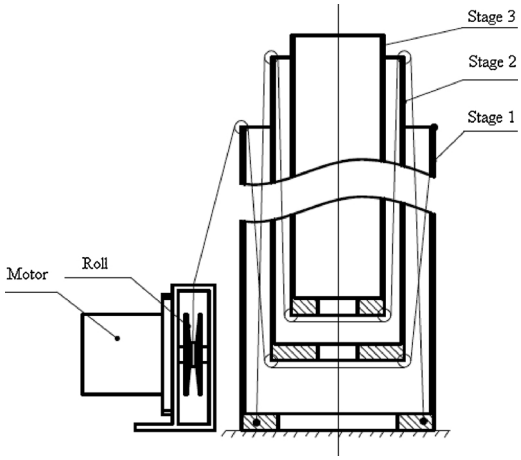

Fig. 10. Lens hood deployment mechanism.

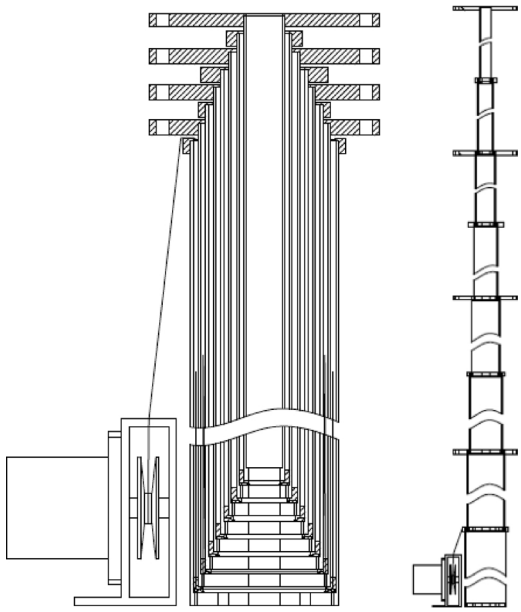

Fig. 11. Folded and extended status of the lens hood.

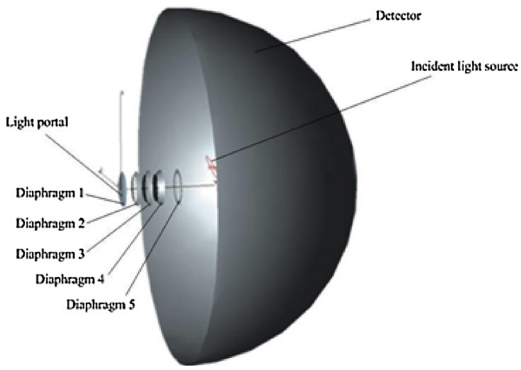

Fig. 12. Overall ray tracing calculation model.

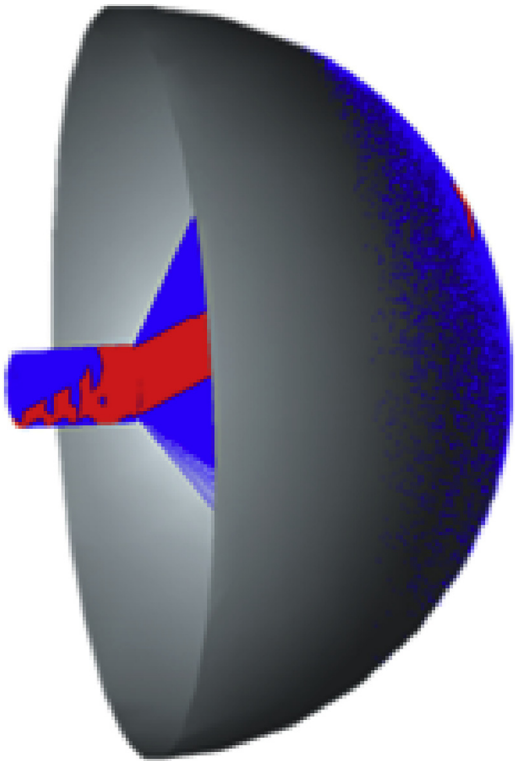

Fig. 13. Trajectories of all rays.

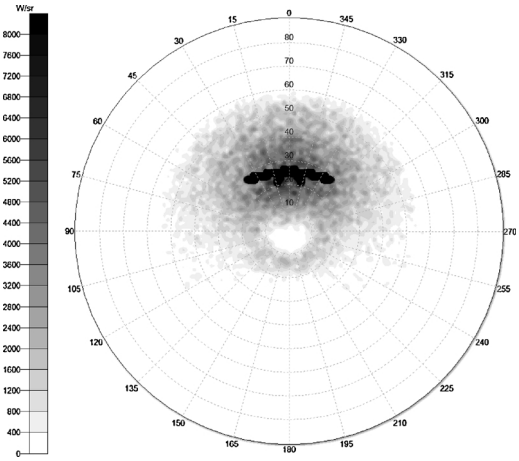

Fig. 14. Distribution of the polar coordinates of the energy received by the detector.

incident zenith angle and the circumferential coordinates represent the incident azimuth.

The detector receives 20,200 W of energy. In total, 8.1% of the energy is reflected. The energy in the lens hood is mainly concentrated in the front of the lens hood, and at the back of Diaphragm 5. This area accounts for 90.4% of the total energy. According to the results of ray tracing, the lens hood design fulfills the objective of reflecting the majority of sunlight out of the lens hood system or move the light forward to the front of the lens hood.

4.2. Heat flux analysis

In any case, the lens hood can't inhibit all of the incident energy, so there will always be a part of the incident energy through the camera aperture into the optical system. The thermal analysis and calculation is performed with the space system thermal module of Siemens NX software. The procedures include pretreatment, solution and post-processing. The calculation conditions are the same as in Section 4.1. The finite element model of the camera aperture heat flux analysis is shown in Fig. 15.

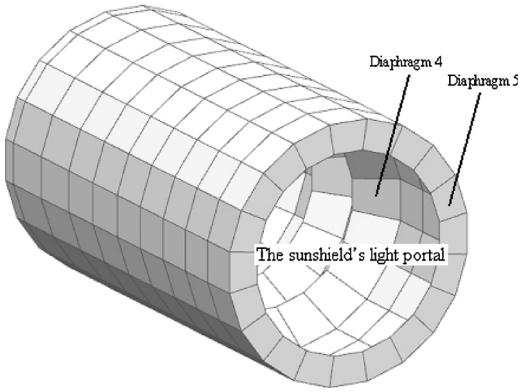

Fig. 15. Finite element model of the camera aperture heat flux analysis.

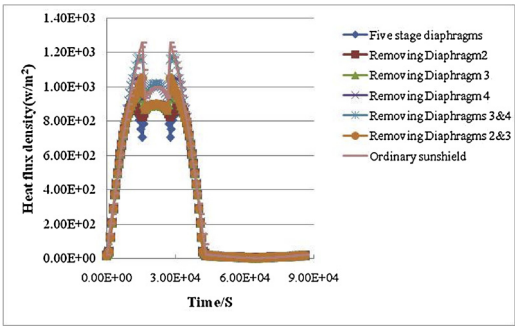

Fig. 16. Heat flux densities of the camera aperture in different models.

Table 2
Statistics on the heat flux densities of the camera aperture.

No.	Name	Average heat flux density (w/m^2)	Peak heat flux density (w/m^2)
1	Five stage diaphragms	341	897
2	Removing Diaphragm 2	346	898
3	Removing Diaphragm 3	357	968
4	Removing Diaphragm 4	382	1050
5	Removing Diaphragms 3&4	398	1170
6	Removing Diaphragms 2&3	362	1050
7	Ordinary lens hood	401	1260

Fig. 16 describes the heat flux densities of the aperture in different models. Table 2 lists the statistics of the heat flux densities of the aperture.

As shown in Table 2, the diaphragm lens hood camera has much lower average and peak heat flux densities than the ordinary lens hood. Generally speaking, the fewer the diaphragm stages, the denser the heat flux at the aperture.

4.3. Modal analysis

This author carries out a system-level modal analysis of the prototype, which probes into the first-order mode to the ten-order mode. The analysis is to verify whether the system mode of the prototype satisfies the dynamic stiffness requirement of the transmitting platform of no less than 30 Hz. The analysis and calculation is performed with the NX Nastran of Siemens NX software. The procedures include pretreatment, solution and post-processing.

The overall finite element model, as shown in Fig. 17, is established according to the structural characteristics of the camera and the needs of mechanical analysis.

See Table 3 for the statistics of the overall analysis.

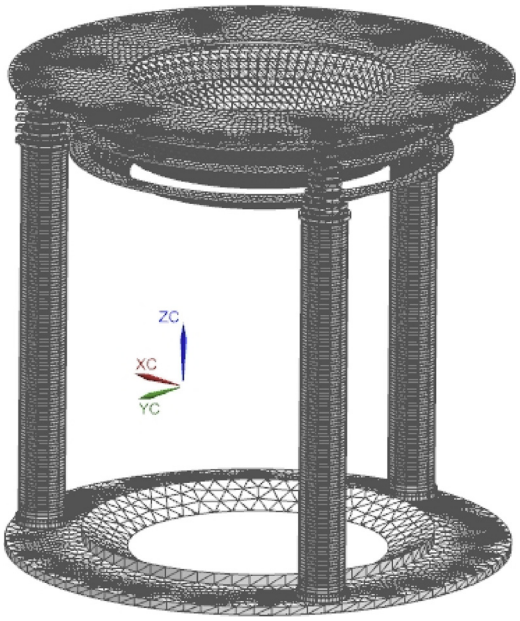

Fig. 17. Overall finite element model.

Table 3
Statistics of the modal analysis.

No.	Mode	Analysis results (Hz)	Vibration mode	Level of satisfaction
1	The 1 st order	34.86	Vibration along the x-axis	Satisfied
2	The 2nd order	35.01	Vibration along the y-axis	Satisfied
3	The 3rd order	40.11	Turning around the z-axis	Satisfied
4	The 4th order	46.41	Vibration along the z-axis	Satisfied
5	The 5th order	49.74	Local vibration of Diaphragm 1	Satisfied
6	The 6th order	98.49	Local vibration of Diaphragm 1	Satisfied
7	The 7th order	132.33	Local vibration of Diaphragm 2	Satisfied
8	The 8th order	144.16	Local vibration of Diaphragm 2	Satisfied
9	The 9th order	152.76	Local vibration of Diaphragm 3	Satisfied
10	The 10th order	164.74	Local vibration of Diaphragm 3	Satisfied

5. Test validation

5.1. Functional verification

The prototype was installed and debugged in the laboratory, and then assembled with the supporting test tools. The lens hood was placed vertically and off-loaded gravity with the test tools. In this state, this author conducted functional verification of the lens hood. The test system is displayed in Fig. 18.

In addition, the compressed and deployed state heights of the prototype are measured to obtain the expansion ratio. The results in Table 4 demonstrate that the prototype satisfies the design requirements.

5.2. Mechanical test verification

The dynamic stiffness characteristics of the lens hood assembly were verified by the modal test in the state of compression locking. In order to verify whether the lens hood meets the dynamic stiffness requirements in the low frequency range, this author carried out a characteristic scanning test at 0–200 Hz. The conditions of the mechanical test are shown in Table 5.

Figs. 19–21 show the curves and Table 6 shows the statistics of the characteristic scanning test for the lens hood. It can be inferred that the dynamic stiffness of the lens hood meets the requirements and the simulation results are in good agreement with the test results.

6. Conclusion

Based on the characteristics of the geostationary optical remote sensor, this paper analyzes the typical working conditions of the

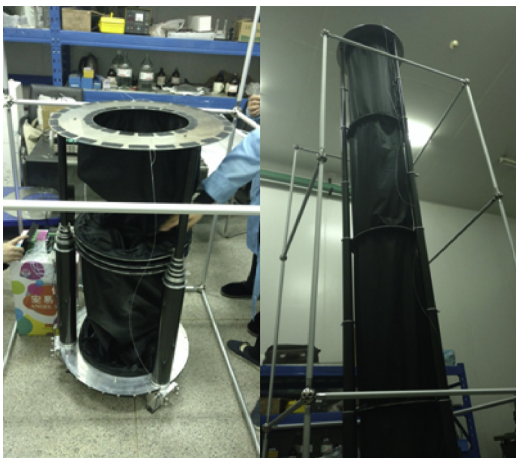

Fig. 18. Functional test system.

Table 4
Prototype measurement results.

No	Design goals	Measurement result	Level of satisfaction
1	Compressed state height ≤0.6m	Compressed state height: 0.588m	Satisfy
2	Deployed state height: ≥3.6m	Deployed state height: 3.612m	Satisfy
3	Expansion ratio: ≥6	Expansion ratio: 6.143	Satisfy

Table 5
Mechanical test conditions.

Direction	Frequency range (Hz)	Acceleration amplitude (g)
X, Y, Z	5-200	0.1
Scanning frequency	In each direction: 2Oct/min	

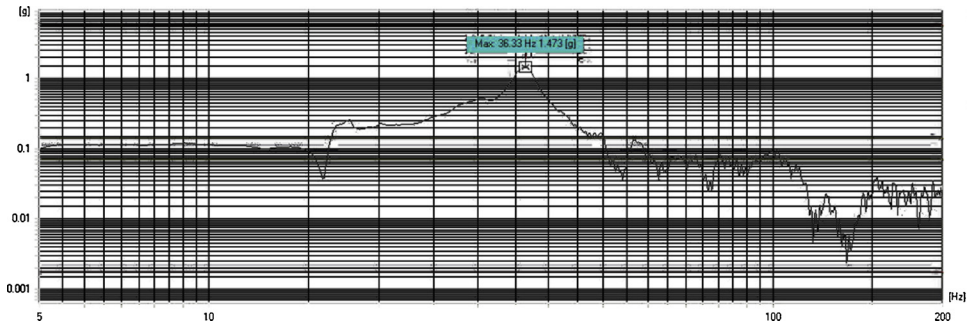

Fig. 19. X-axis test curve.

remote sensor in orbit, clearly defines the external heat flux conditions of the camera, and puts forward the plan of a deployable heat dissipation lens hood at the light aperture of the camera. The simulation results indicate that more than 98% of the incident light can be reflected out of the lens hood system or moved to the front by the proposed lens hood.

Furthermore, camera with the diaphragm lens hood has a much lower average and peak heat flux densities than the ordinary lens hood. With the fundamental frequency of 36.33 Hz, the main structure of the lens hood satisfies the dynamic stiffness requirement.

Acknowledgments

This research was supported by a National Natural Science Foundation of China project, which is a part of an innovation project. All the experiments were carried out in the space test hall of the Changchun Institute of Optics, Fine mechanics and Physics, Chinese Academy of Sciences.

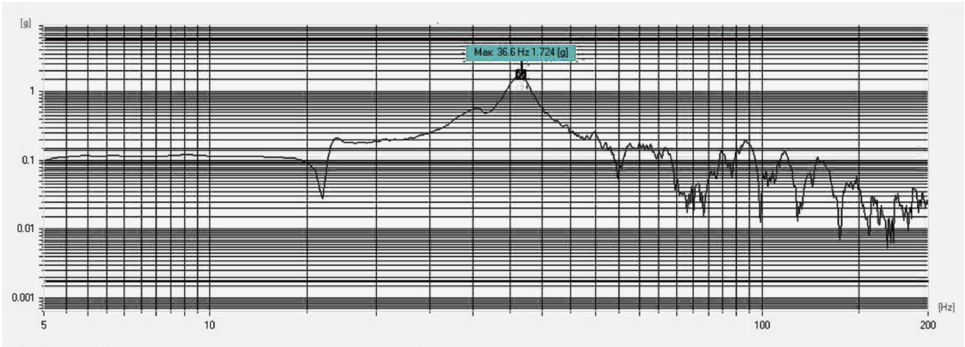

Fig. 20. Y-axis test curve.

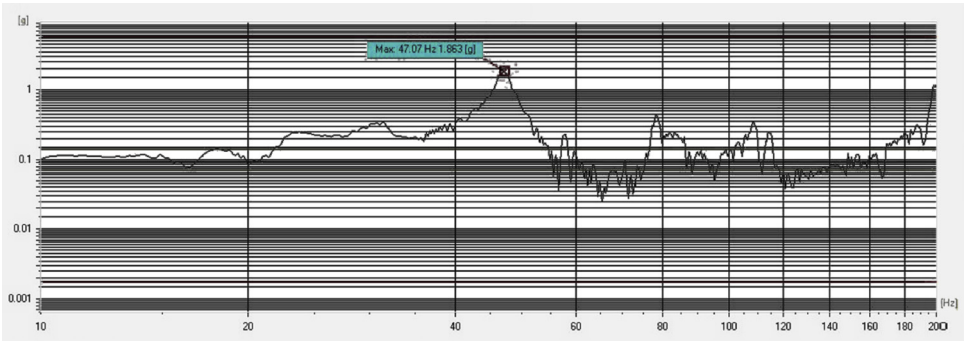

Fig. 21. Z-axis test curve.

Table 6
Mechanical test statistics.

No	Direction	Fundamental frequency (Hz)
1	X	36.33
2	Y	36.60
3	Z	47.07

References

[1] P. Mazzinghi, V. Bratina, D. Ferruzzi, L. Gambicorti, et al., Deployable, lightweight and large aperture spaceborne telescope for LIDAR based earth observations, Proc. SPIE 6750 (2007) 67500X-1–67500X-10.
[2] Davide Piovesan, Mirco Zaccariotto, Carlo Bettanini, et al., Design and validation of a carbon-fiber collapsible hinge for space applications: a deployable boom, J. Mech. Rob. 8 (2016) 031007-1–031007-11.
[3] N. Knight, K. Elliott, J. Templeton, et al., FAST mast structural response to axial loading: modeling and verification, AIAA/ASME/ASCE/AHS/ASC Structures, Structural Dynamics and Materials Conference, (2013), pp. 1–31.
[4] Rolf Danner, Sergio Pellegrino, Dean Dailey, Geoff Marks, Precision-deployable, Stable, Optical Benches for Cost-Effective Space Telescopes, Northrop Grumman Aerospace Systems, 2012.
[5] Justin J. Rey, Allan Wirth, Andrew Jankevics, et al., A deployable, annular, 30m telescope, space-based observatory, Proc. SPIE vol. 9143, (2014) 914318-1–914318-14.
[6] D. Entekhabi, E.G. Njoku, P.E.O. Neill, et al., The soil moisture active passive (SMAP) mission, Proc. IEEE 98 (5) (2010) 704–716.
[7] Xiaokai Wang, Houfei Fang, Bei Cai, Xiaofei Ma, Deployment simulation of a deployable reflector for earth science application, Proc. SPIE 9639 (2015) 96391F1–8.
[8] G. Kotova, M. Verigin, G. Zastenker, et al., Bow shock observations by Prognoz–Prognoz 11 data: analysis and model comparison, Adv. Space Res. 36 (10) (2005) 1958–1963.
[9] RandyA. Kimble, M. Begoña Vila, Julie M.Van Campen, Stephan M. Birkmann, Brian J. Comber, et al., Cryo-vacuum testing of the JWST integrated science instrument module, Proc. SPIE 9904, Space Telescopes and Instrumentation 2016: Optical, Infrared, and Millimeter Wave, (2016), pp. 408–420.
[10] N.S. Andreas, Space-based infrared system (SBIRS) system of systems, Aerospace Conference, 1997. Proc. IEEE, (1997), pp. 429–438.
[11] M. Wooldridge, N.R. Jennings, D. Kinny, The Gaia methodology for agent-oriented analysis and design, Auton. Agents Multi-Agent Syst. 3 (3) (2000) 285–312.
[12] M. Roman, C. Hess, R. Cerqueira, et al., Gaia: a middleware infrastructure to enable active spaces, IEEE Pervasive Comput. 1 (4) (2010) 74–83.
[13] Roberto Gardi, Giulia Pica, Realization and preliminary tests on an innovative deployable structure for a high resolution telescope for microsatellite, SPIE vol. 5570, (2004) 411–422.
[14] Giulia Pica, Luca Ciofaniello, et al., High resolution deployable telescope for satellite application, SPIE vol. 5234, (2004) 531–538.
[15] David W. Robinson, RyanS. McClelland, Mechanical overview of the International X-Ray observatory, IEEEAC, (2009) Version 1:1-10.
[16] C. Mackenzie, B. Sweetman, Snakes and lasers, Aviat. Week Space Technol. 174 (23) (2012) 16–22.
[17] Peter A. Warren, Mark J. Silver, Benjamin J. Dobson Jret al., Experimental characterization of deployable outer barrel assemblies for large space telescopes, Proc.

SPIE 8860 (886008) (2013) 1–13.
[18] Peter A. Warren, Mark J. Silver, Benjamin J. Dobson, Lightweight optical barrel assembly structures for large deployable space telescope, Proc. SPIE 7436 (74360B) (2009) 1–8.
[19] Joseph N. Footdale, Thomas W. Murphey, Mechanism design and testing of a self-deploying structure using flexible composite tape springs, Proceedings of the 42nd Aerospace Mechanisms Symposium, (2014), pp. 497–510.
[20] J.B. Breckinridge, Geometry attained by pressurized membranes, Proc. SPIE – Int. Soc. Opt. Eng. 3356 (1998) 747–757.
[21] M. Schenk, S.G. Kerr, A.M. Smyth, S.D. Guest, Inflatable cylinders for deployable space structures, Proceedings of the First Conference Transformables 2013 in the Honor of Emilio Perez Pinero, (2013), pp. 1–6.
[22] Veal, G., Palisoc, A. Derbes, W., (2004), Deployable inflatable boom and methods for packaging and deploying a deployable inflatable boom. United States Patent 6786456.
[23] Jian-zheng Wei, Simulation and experiment for inflatable control deployment of rolled booms, 51st AIAA/ASME/ASCE/AHS/ASC Structures, Structural Dynamics, and Materials Conference, (2010), pp. 1–11.
[24] J.C.H. Yee, O. Soykasap, S. Pellegrino, Carbon fibre reinforced plastic tape springs, Gossamer Spa, Collection of Technical Papers-AIAA /ASME /ASCE /AH S /ASC S Tructures, Structural Dynamics and Materials Conference (2004) 3305–3313.
[25] Lambda Research Corporation.TracePro_Brochure_v2014.pdf.[DB/OL].https://www.lambdares.com/tracepro/,2014.